The Astrophysical Journal, 903:134 (15pp), 2020 November 10 https://doi.org/10.3847/1538-4357/abbb92

Measuring the Variability in K2 Optical Light Curves of 3C 273 and Other Fermi Active Galactic Nuclei in 2015–2017

Michael Carini[1], Ann E. Wehrle[2], Paul J. Wiita[3], Zoë Ward[4], and Kennedy Pendleton[4]
[1] Western Kentucky University, Department of Physics and Astronomy, 1906 College Heights Boulevard, Bowling Green, KY 42101, USA
[2] Space Science Institute, 4765 Walnut Street, Suite B, Boulder, CO 80301, USA
[3] The College of New Jersey, Department of Physics, P.O. Box 7718, Ewing, NJ 08628-0718, USA
[4] Western Kentucky University, Carol Martin Gatton Academy of Mathematics and Science in Kentucky, 1906 College Heights Boulevard, Bowling Green, KY 42101, USA
Received 2020 July 30; revised 2020 September 23; accepted 2020 September 23; published 2020 November 11

Abstract

We characterize the variability in nearly continuous optical observations of the bright radio-loud quasar 3C 273 and nine additional active galactic nuclei detected with the Fermi Gamma-ray Space Telescope Large Area Telescope (Fermi-LAT). Optical observations were obtained during the K2 mission with the Kepler spacecraft for periods of 49 to 83 days conducted with $\simeq$1 minute (short) or $\simeq$30 minutes (long) cadences in 2015–2017. 3C 273 was quiescent during the course of the observations, varying by only a factor of 1.02. Three objects, PKS 0047+023, PKS 1216-10, and PKS B2320-035, were active, varying by factors of 1.8–3.4. Six other objects were comparatively quiet, varying by factors of less than 1.4. Power spectral densities (PSDs) were calculated for each object. Overall, the slopes of most PSDs, as well as those we reported in an earlier paper, were in the range −2.0 to −2.7 and are consistent with those produced by turbulence in the relativistic jet, and not by "hot spots" in the disk emission. Mechanisms operating in the jet other than turbulence, such as "mini-jets" or "jet-in-jets", may also produce the observed range of PSD slopes. Both accretion disk and jet models are plausible origins for the 3C 273 optical variability during the K2 observations.

Unified Astronomy Thesaurus concepts: Active galactic nuclei (16); Active galaxies (17); Jets (870)

1. Introduction

3C 273, the first quasar discovered, is the archetype of bright quasars. It has a prominent optical and radio jet on kiloparsec scales. The superluminal parsec-scale jet is inclined about $9° \pm 2°$ to our line of sight (Jorstad et al. 2017). Only a few years after its discovery, it was detected at γ-ray bands by *COS-B* (Swanenburg et al. 1978). Extensive monitoring over the past 50 years has shown that it is variable at all wave bands (see, e.g., the reviews by Türler et al. 1999 and Soldi et al. 2008 with the accompanying database http://isdc.unige.ch/3c273/, and Chidiac et al. 2016 and references therein). The optical emission is a combination of broad emission lines and thermal continuum (the optical-ultraviolet "big blue bump") from its accretion disk and hot corona, as well as nonthermal synchrotron continuum emission from a "mini-blazar" nucleus and jet (Schmidt & Smith 2000). The fraction from each component changes with time, and the nonthermal contribution has been variously estimated as $\sim$10% (Impey et al. 1989) and 25%–50% (Li et al. 2019). Work by Chidiac et al. (2016) and Fernandes et al. (2020) concluded that the optical emission is dominated by the disk. Reverberation mapping by Li et al. (2020) has shown that the Hβ emission lines responded to changes in the *V*-band continuum with a lag of $\approx$195 days, about 15% larger than that found by Zhang et al. (2019) using overlapping data sets obtained in 2008–2018.

Continuous optical monitoring on timescales from minutes to months became possible with the advent of the K2 mission using the Kepler spacecraft. K2 observed 19 campaigns in 10° fields along the ecliptic plane, including targeted observations of hundreds of quasars and other active galactic nuclei (AGNs). We have reported previously on simultaneous K2 and Fermi Gamma-ray Space Telescope Large Area Telescope (Fermi-LAT) observations of the well-known BL Lac object and binary black hole candidate OJ 287 (Wehrle et al. 2019, hereafter Paper I)) and eight other γ-ray blazars. In this paper, we present simultaneous K2 and Fermi-LAT observations of 3C 273 and nine more γ-ray blazars. A forthcoming third paper will present results for the remaining 13 sources in the sample as well as for the repeat observations of eight sources from Paper I and this paper, including OJ 287.

In Section 2 we describe the selection of γ-ray blazars in K2 Campaigns 7, 8, 10, 12, and 13. In Section 3 we briefly describe the K2 observations, how the data were reduced, and how the light curves were analyzed. We give the results of these K2 optical observations, including the power spectral densities (PSDs), in Section 4 and describe the Fermi-LAT data and our analysis of them in Section 5. In Section 6 we discuss our results, and in Section 7 we summarize our conclusions.

2. The Blazar Sample Selection

We initially chose 12 γ-ray blazar targets (Table 1) as in Paper I by searching the Fermi-LAT Second AGN Catalog (2LAC; Ackermann et al. 2011) for the optically brightest blazars in the K2 Campaigns 7, 8, 10, 12, and 13 fields (programs GO7015, GO8005, GO10005, GO12081, and GO13081 respectively, led by principal investigator A. Wehrle). Seven blazars overlapped with the infrared and optically bright samples selected by programs GO7026, GO10057, GO12094, and GO13094 that were led by principal investigator M. Carini. Updated γ-ray names from the Fermi-LAT Third Source Catalog (3FGL; Acero et al. 2015) are used in Table 1. The 12 γ-ray blazars in the five fields had estimated K2 optical magnitudes K_p in the 420–900 nm band from 12.737 to 21.0 in the K2 EPIC catalog (Huber et al. 2016; Huber & Bryson 2018 and references therein), which was generally drawn from the USNO-B and Sloan Digital Sky Survey

Table 1
Targets

Name	EPIC ID	Fermi-LAT Name	K_p[a]	z	Class	K2 Program	Campaign Field	Notes
PKS B1908-201	217700467	3FGL J1911.2-2006	16.471	1.12	FSRQ	GO7015	7	…
1H 1914-194	218129423	3FGL J1917.7-1921	15.341	0.137	BL Lac	GO7015, GO7026	7	…
TXS 1920-211	217154395	3FGL J1923.5-2104	16.732	0.874	FSRQ	GO7015, GO7026	7	1
PKS B1921-293	229228355	3FGL J1924.8-2914	16.410	0.353	BL Lac[b]	GO7015	7	…
PKS 0047+023	220299433	3FGL J0049.7+0237	18.84	(>0.55)[c]	BL Lac	GO8005	8	…
1RXS J120417.0-070959	201079736	3FGL J1204.3-0708	16.305	0.184	BL Lac[d]	GO10005, GO10057	10	…
PKS 1216-010	201375481	3FGL J1218.4-0121	16.626	0.415	BL Lac[b]	GO10005, GO10057	10	…
3C 273	229151988	3FGL J1229.1+0202	12.737	0.159	FSRQ	GO10005, GO10057	10	…
1RXS J121946.0-031419	201247917	3FGL J1219.7-0314	17.091	0.299	BL Lac	GO10005	10	…
PKS B2320-035	246289180	3FGL J2323.5-0315	18.362	1.41	FSRQ	GO12081, GO12094	12	…
PKS B2335-027	246327456	3FGL J2338.1-0229	18.318	1.072	FSRQ	GO12081	12	…
87 GB 045310.1+265754	251456988	3FGL J0456.3+2702	21.000	…	FSRS	GO13081	13	1

Notes. 1. Target omitted from final sample due to poor K2 data quality.
[a] Kepler magnitude as tabulated in the EPIC catalog, which was compiled largely from ground-based catalogs USNO-B and SDSS.
[b] Also classified as a highly polarized quasar (HPQ).
[c] The redshift lower limit was estimated from nondetection of starlight by Paiano et al. (2017), see their discussion of its featureless spectrum. A redshift of 1.44 in the SDSS catalog was estimated using multiband photometry from the SDSS.
[d] Classified as BL Lac with the host galaxy clearly visible in the digitized POSS image.

(SDSS) catalogs. 3C 273 is by far the brightest, with $K_p = 12.737$. Two targets, TXS 1920-211 (EPIC 217154395) and the flat-spectrum radio source (FSRS) 87 GB 045310.1+265754 (EPIC 251456988), were dropped from the sample because their K2 data quality was poor (see below). In our final sample of 10 targets, 6 are classed as BL Lacertae objects (BL Lacs) and 4 as flat-spectrum radio quasars (FSRQs).

3. K2 Observations, Data Reduction, and Analysis

A journal of the K2 and Fermi-LAT observations is given in Table 2. Campaigns 7 and 13 were uneventful. Campaign 8 lost data for one day on 2016 February 1–2 when the spacecraft dropped out of fine lock control. Campaign 10 had two anomalies, as described in the K2 Data Release Notes https://keplergo.github.io/KeplerScienceWebsite/k2-data-release-notes.html#k2-campaign-10. The first anomaly was that K2 had a pointing error of 3.5 pixels (14″) at the start of the campaign, which was corrected after 6 days. Data from the first 7 days of Campaign 10 are designated Campaign 10a and Campaign C101 in the MAST archive, while subsequent data are designated 10b(1) and 10b(2) and are indicated in the MAST archive as C102. The second anomaly was the failure of Module 4, which led to a 14-day gap between 2016 July 20 and 2016 August 3. Because 3C 273 was a high-priority target for K2, the K2 Project GO Office astronomers had made a special, larger than normal, pixel mask for it; hence, its light curve during the time that K2 was mispointed for 7 days was recoverable. We used the continuous 49-day light curve (10b(2)) for 3C 273 and the other three targets in Campaign 10. Campaign 12 had a five-day gap while the spacecraft was in safe mode between 2017 February 1 at 15:06 UTC and 2017 February 6 at 20:47 UTC.

Although most of the long-cadence light curves yielded ∼3400 29.4-minute ("30-minute") samples, the much shorter campaign 10b(2) yielded ∼2400 data points. As discussed in more detail in Paper I, to correct for the photon-pressure-induced drift of the spacecraft and the near-periodicity (at approximately 6 or 12 hours) of the spacecraft thruster (Van Cleve et al. 2016), we used count data that were corrected using the EVEREST algorithm developed by Luger et al. (2016, 2018). Thermal effects also impact the measurements, albeit to a much smaller extent, and basically only during the first couple of days at the beginning of each campaign pointing. As these instrumental effects are not removed by the EVEREST postprocessing, we identified and removed these anomalous data.

Table 2
Dates of K2 and Fermi-LAT Observations

K2 Campaign	Dates	MJD	Duration
7	2015 Oct 4—2015 Dec 26	57299–57382	83 days
8	2016 Jan 4—2016 Mar 23	57391–57470	79 days
10a	2016 Jul 6 —2016 Jul 13	57575–57582	7 days
10b(1)	2016 Jul 13—2016 Jul 20	57582–57589	8 days
10b(2)	2016 Aug 3—2016 Sep 20	57603–57651	49 days
12	2016 Dec 15—2017 Mar 4	57737–57817	81 days
13	2017 Mar 8—2017 May 27	57820–57901	81 days

Early community work with the standard Kepler pipeline products revealed that the standard Kepler processing had issues with AGN light curves (Wehrle et al. 2013; Revalski et al. 2014), and it became clear that better analysis techniques were required, as standard pipeline output for AGNs often removes true astrophysical brightness variations while trying to eliminate instrumental effects. As in Paper I, we examined the light curves produced by the standard processing (SAP, PDCSAP), the K2SFF processing (Vanderburg & Johnson 2014, and later updates online at MAST), and the EVEREST processing (Luger et al. 2016, 2018). In the current source sample, we used the EVEREST light curves because they had the fewest remaining clear instrumental errors (thermal recovery drifts at the beginnings of campaigns, isolated single low points, and residual "sawtooth" amplitude variations at 6- and 12-hour intervals). We compared the light curves of several nearby objects on the same CCD module to see if there were flux variations in common that were not removed by the processing, as these could be mistaken for true astrophysical variations if we had examined only the light curve of our target. In one case, stars on the same CCD channel as PKS 0047+023 (EPIC 220299433) showed a common rise and fall of ∼3% in amplitude over 15–20 days near the end of the campaign. During this time, PKS 0047+023 varied by 40%. The common bump in the stellar light curves indicated that an instrumental effect had not been completely removed by EVEREST, and this effect may have contributed to the relatively high dispersion in the PSD of this source at log $\nu < -6.0$. Two targets fell on a module affected by medium nonlinear amplifier ("Moiré") effects (Kolodziejczak et al. 2010; see also Table 13 of the Kepler Instrument Handbook, Van Cleve & Caldwell 2016). Fortunately, our detailed examination of the amplitude variations of the targets that fell on the medium Moiré-affected channel, EPIC 217700467 and 201375481, showed no visible evidence of Moiré distortions. We looked for, but did not see, "rolling band" effects, which are caused by broad temperature-sensitive noise aliased to near-zero frequency (Kepler Instrument Handbook, Section 6.7.1).

Our observations of 3C 273 using long-cadence data achieved a noise level (standard deviation) after EVEREST processing of 18 ct s^{-1} ($\sim$0.028%). All the other targets were much fainter and yielded noise levels of 3–28 ct s^{-1}, while the brightnesses were 511 to 15,424 ct s^{-1}. These noise measurements were made during 0.5-day intervals when the light curves exhibited variations below 1%. The 3C 273 short-cadence pipeline data were retrieved from the MAST archive for custom EVEREST processing (not all K2 target short-cadence data have been processed through EVEREST by R. Luger and colleagues and archived on MAST). The complete short-cadence light curve of 3C 273 yielded 101,520 one-minute samples, of which $\sim$76,000 data points were in the longest segment, Campaign 10b(2). After removing poor quality data, we used 66,371 one-minute samples. The short-cadence data set was $\sim$30 times larger than the long-cadence data set, which was created by averaging the short-cadence data before pipeline processing and correction for instrumental effects. Following advice from R. Luger, detrending was accomplished with the "everest.Detrend" routine, using the same aperture and kernel parameters as for the long-cadence data. The short-cadence observation was broken up into 30 segments for the detrending, consistent with the number of breakpoints used for all other short-cadence observations detrended with the EVEREST software (Luger et al. 2018). Cotrending basis vector (CBV) correction was applied using the long-cadence CBVs, and only one CBV was used, again consistent with all other EVEREST-reduced data in the MAST archive. The short-cadence noise levels were 49 ct s^{-1} compared to the long-cadence noise levels of 18 ct s^{-1}, on K2 BJD 2806-2806, during 24 hours where the source varied less than during the rest of the campaign. The K2 light curves do not have absolute calibration. We obtained photometry of 3C 273 in 2016 with the 1.3 m Robotically Controlled Telescope (RCT) available to one of us (Carini). Accordingly, to place the K2 data in recent historical context, we scaled the ground-based data to the K2 count rate at the beginning of the K2 Campaign 10b(2) and show the overall optical light curves in 2016 in Figure 1.

Examination of the K2 pipeline and EVEREST light curves and the full K2 postage-stamp apertures used in processing for each target revealed problems with two targets, TXS 1920-211 (EPIC 217154395) and 87 GB 045310.1+265754 (EPIC 251456988). TXS 1920-211 ($K_p = 16.73$) is in a crowded field including a brighter object ($K_p = 15.3$) within two pixels and several other objects (with $K_p = 16.0$ to 18.1) within four pixels. Custom processing with smaller target apertures and carefully selected background apertures showed that the emission from the target was not separable from the other objects nearby. Hence, we omitted TXS 1920-211 from further consideration. Similarly, when we examined the data for the 21st magnitude target 87 GB 045310.1+265754 (EPIC 251456988), we found that its signal was not reliably measurable above the background levels in the aperture. Therefore we also omitted 87 GB 045310.1+265754 from further consideration. The final sample contained 10 targets, all with good-quality data.

4. K2 Optical Results

The K2 EVEREST light curves for our targets are shown in the top panels of Figures 2–5. Key features of these light curves are given in Table 3. During the K2 observations, the greatest variation detected was a factor of 3.37 for PKS 0047+023. The least variation, a factor of 1.02, was seen in 3C 273. Variations by factors of 1.11 to 2.41 were detected in six objects. The remaining two targets showed variations of a factor of 1.06.

We formed PSDs from the Fourier transforms of the light curves for each target in a manner identical to Paper I, which we refer to for additional details. These PSDs are usually characterized by red noise, with $P(\nu) \propto \nu^{\alpha}$, with $\alpha < 0$, for $\nu < \nu_b$; above this break frequency, it has a white-noise character ($\alpha = 0$) that is characteristic of being dominated by measurement errors. To minimize the red leak (transfer of variability power from low to high frequencies), we computed the PSDs after end-matching the data to remove any linear trend and then convolved them with a Hamming window function. To best estimate the PSD slopes, we then binned the logarithm of the power in intervals of 0.08 in log ν and found a linear fit to the portion of the PSD displaying power-law behavior (bottom panels of Figures 2–5). Error bars in the PSD plots represent the rms scatter in the data points in each bin, and where there is only one point per bin, no error bar is shown. The uncertainty quoted for the measurement of the PSD slope is the uncertainty in the unweighted linear fit to the binned PSD. Further study of the PSDs in Paper I and in this paper led us to determine that there existed a sweet spot in the power laws in the frequency range of log $\nu = -5.0$ to -6.4, where the data are more abundant, well-sampled, and less noisy than at higher and lower frequencies. In order to avoid the fit being unduly affected by points at the lowest frequencies, we set the lower limit of the sweet spot to be log $\nu = -6.4$. We fit eight of the PSDs from this paper in that frequency range (Table 3) and refit the PSDs from Paper I in the same sweet-spot frequency range (Table 4). We fit four PSDs in the slightly reduced frequency range of log $\nu = -5.0$ to -6.2 for the targets observed in the short Campaign 10b(2).

As a test of our PSD computation and to eliminate the possibility of instrumental effects on the PSD slope, we determined the PSD for a nonvariable white dwarf observed during the Kepler mission: KIC 6212123. This is a DA D-type white dwarf (Doyle et al. 2017) with an SDSS r magnitude of 16.996. The PSD was calculated for this source in a manner identical to the way we calculated the PSD for our blazar sample objects. We determined the PSD for the source over four different quarters (2–5) with the source falling on different CCD channels in each quarter (23, 39, 63, and 47,

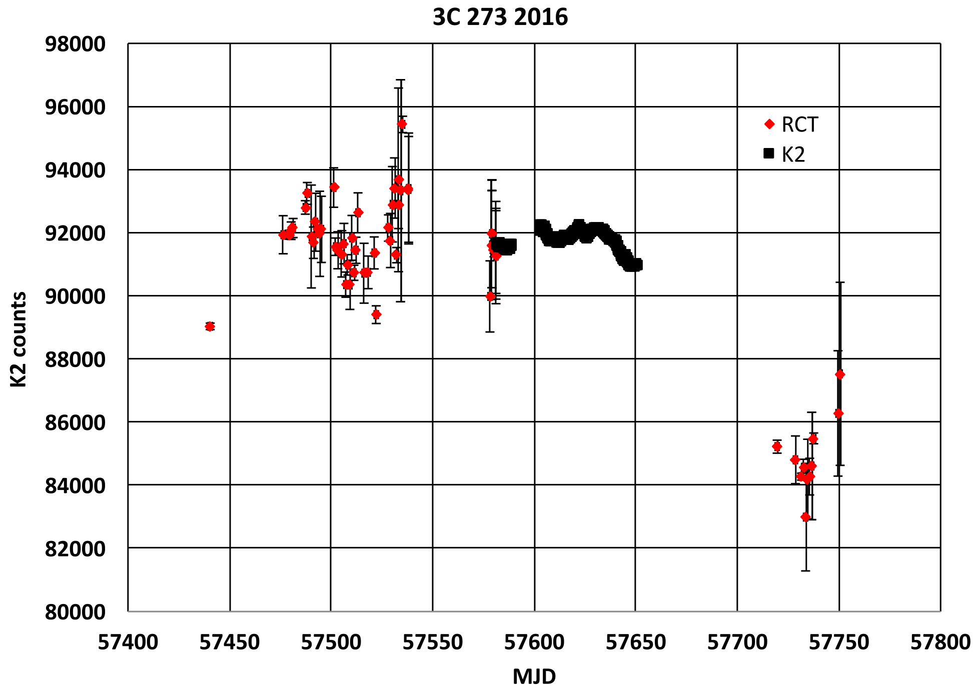

Figure 1. Combined ground-based and K2 (EVEREST-processed) light curve of 3C 273 in 2016. Ground-based *R*-band photometry is from the RCT program led by M. Carini. The *R*-band photometry has been scaled to match the first K2 observation on MJD 57575 (2016 July 6). For reference, 2016 January 1 is MJD 57388.0 and 2016 December 31 is MJD 57754.0.

respectively). In all four quarters, the linear fit to the resulting PSD was consistent with a slope = 0 (white noise), as expected for a presumably nonvarying source. Figure 6 shows all 10 PSDs of the K2 blazar targets, the PSD of the white dwarf during one quarter of Kepler observations, and a PSD of simulated white noise. We also determined the slope of the PSD via the PSRESP method (Uttley et al. 2002) in the sweet spot for the objects in this paper and refit the objects from Paper I in the sweet spot using PSRESP. In addition to an estimate of the slope and its associated uncertainty, PSRESP also calculates a confidence factor describing the acceptability of the fit of the assumed power-law model to the data. We implemented the PSRESP method as described in Paper I.

To see how much the processing methods affected the light curves and PSDs, we analyzed the data from the K2 Project's PDC pipeline, EVEREST (Luger et al. 2016, 2018), and K2SFF (Vanderburg & Johnson 2014 and updates at MAST). Comparison of PSDs resulting from three light-curve processing methods of EPIC 246327456, also known as PKS B2335-027, are shown in Figure 7. This source was chosen because it has the lowest number of counts of any source in our sample; thus we expect any effects due to different processing methods to be most prominent in this object. The PDC, EVEREST, and K2SFF methods yielded sweet-spot slopes of -2.14 ± 0.24, -2.30 ± 0.29, and -1.70 ± 0.19, respectively. We note that the PSD is somewhat curved rather than purely linear in log-log space in our sweet-spot region in this object, especially for the PDC and K2SFF processing. After $\log \nu = -5.5$, the PSD becomes linear in appearance. The slopes for the more restricted range of $\log \nu = -5.5$ to -6.4 were in closer agreement: -2.80 ± 0.32, -2.59 ± 0.64, and -2.52 ± 0.25, respectively. A similar analysis of one of the brightest objects in our sample, EPIC 211991001 (OJ 287), yielded slope values with a total range of 0.12, well within the error bars on the individual slope measurements.

For the short-cadence data on 3C 273, we anticipated that the PSD, as we found in OJ 287, would show a plateau induced by sampling effects between $\log \nu = -4.2$ and -3.8, corresponding to timescales between 4.4 and 1.8 hours. A similar plateau in the 3C 273 PSD did appear. Accordingly, as in Paper I, we used the DFOURT and CLEAN methodology (Roberts et al. 1987; Högbom 1974). The CLEANed PSD had a slope of -2.77 ± 0.12 (Figure 2(b)), almost the same as the OJ 287 short-cadence PSD slope of -2.83 ± 0.08 in a similar frequency range. 3C 273 was brighter than OJ 287 (average count rates of 91,737 versus 17,001 ct s^{-1}), so we expected to be able to track red noise down to shorter timescales in 3C 273; however, this was not the case. The turnover from red noise to white noise occurred at $\log \nu \simeq -3.7$ in 3C 273 and $\log \nu \simeq -2.8$ in OJ 287 (corresponding to timescales of 1.4 hr and 8.4 min, respectively). The turnover to white noise in the SC light curve is at a higher frequency than seen in the LC light curve due to the increased time resolution in the SC light curve. We checked segments of the short-cadence light-curve variations on timescales of a few minutes and verified that blazar-like flares and dips on timescales corresponding to the frequency range between $\log \nu = -3.0$ to -2.7 were indeed missing from the 3C 273 data. It is possible that the difference in the timescale of the onset of white noise between the two blazars has an astrophysical cause, but it is also possible that the differences are due to instrumental effects or are related to the different rest-frames of the emission that we observe in Kepler's broad (4200 to 9000 Å) optical passband.

5. Fermi-LAT Observations

We used the methods described in Paper I, tailored as follows, to reduce the Fermi-LAT data. We processed the Pass 8 data (Atwood et al. 2013) from the Fermi Science Support Center for the five fields with radius 20°. Each Fermi-LAT field was centered on the concurrent K2 campaign field centers, and

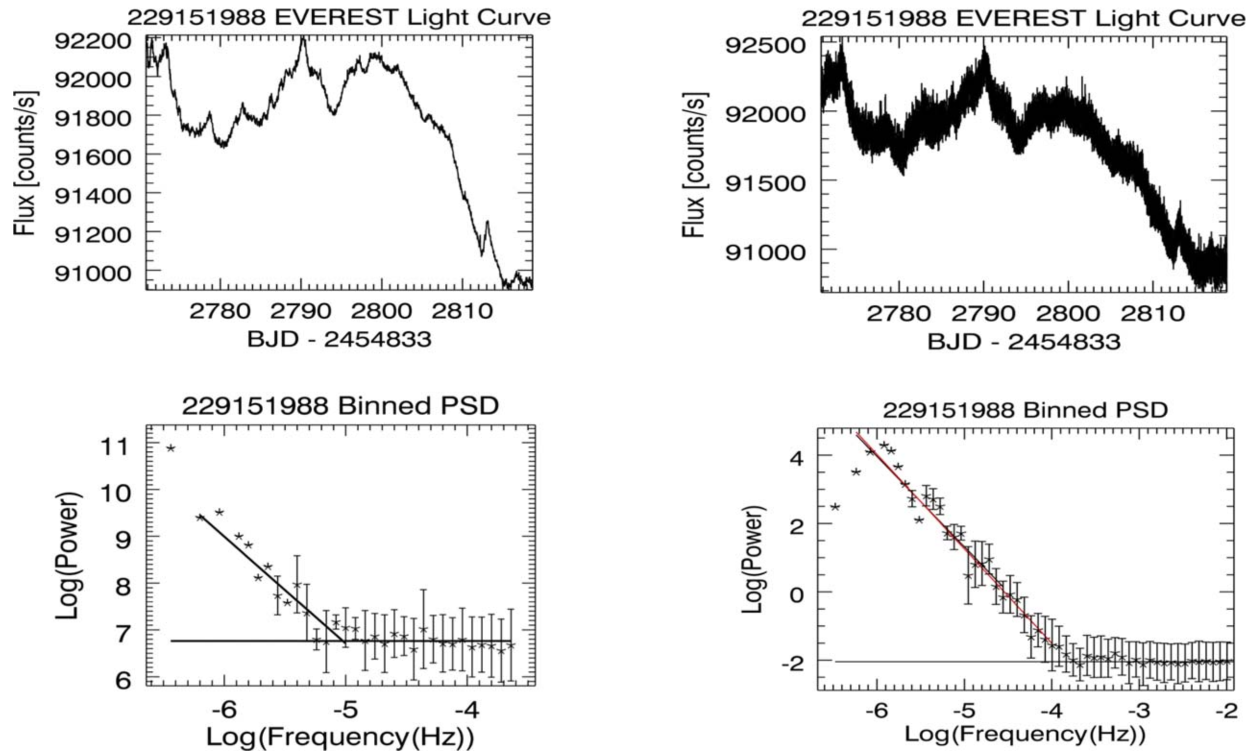

(a - Long Cadence) (b - Short Cadence)

Figure 2. Long- and short-cadence light curves (top left and right) of 3C 273 (EPIC 229151988 and 3FGL J1229.1+0202) as processed by EVEREST and binned power spectral densities (bottom left and right). The PSD slopes of the long- and short-cadence data, -2.43 ± 0.23 and -2.55 ± 0.34, respectively, in the sweet-spot frequency range $\log \nu = -5$ to -6.2, agree within the errors. The PSD slope of the short-cadence data, -2.77 ± 0.12, fit to the excellent quality data over the wider red-noise frequency range extending from $\log \nu = -4$ to -6.2 (in red), is steeper than the slope fit to the narrower sweet-spot range (in black); see the large online figure for details.

was large enough to include all the targets observed with K2. The time ranges (49-83 days) spanned the corresponding K2 observing dates. We used version v10r0p5 of the Fermi Science Tools. We selected only "SOURCE class" events (parameters "evclass = 128, evtype = 3") with energy range 0.1–500 GeV and with the maximum zenith angle set to 90°. Binned likelihood was used for the two fields that included parts of the Galactic Plane (K2 Campaigns 7 and 13) and unbinned likelihood for the other campaigns.

As in Paper I, for models of diffuse emission, we used gll_iem_v06.fits and iso_P8R2_SOURCE_V6_v06.txt. The spectral parameters of the 3FGL (Acero et al. 2015) were used in applying the python script "make3FGLxml.py" to "gll_psc_v16.fit") as starting values for the likelihood calculations for the K2 targets in our field as well as other bright sources within a 30° radius. Because only sources that were in the 3FGL appeared close to our targets, using the 4FGL source list (Abdollahi et al. 2020) would not have made a significant difference in our results. We calculated upper limits at the 95% confidence level for targets not detected with the initial processing using the *fermiPy UpperLimits* scripts (Wood et al. 2017, https://github.com/fermiPy/fermipy/tree/master/fermipy) in the energy range 0.1–300 GeV. For the targets with upper limits, we extracted the Fermi-LAT data again with a smaller radius 15°and included bright sources within 25° radius to obtain convergence of the likelihood calculations, using the methods in the "Likelihood with Python" tutorial at https://fermi.gsfc.nasa.gov/ssc/data/analysis/scitools/python_tutorial.html. We computed power-law spectral indices, fluxes, and test statistic (TS) values for each K2 target. Of the 10 K2 targets, we detected 6 above TS = 25 ($\gtrsim 5\sigma$) (the detected blazars in Paper I all had TS > 17, while those in this paper had TS > 25), and we found upper limits for the remaining 4 targets (Table 5). Combined with the nine blazars in Paper I, our detection rate with Fermi-LAT was 63%, yielding a roughly 60:40 chance of detection with Fermi-LAT of these types of optically bright γ-ray blazars during randomly occurring 2-3 month timespans. We found no evidence of variability in the online database for the Fermi All-sky Variability Analysis (Abdollahi et al. 2017, https://fermi.gsfc.nasa.gov/ssc/data/access/lat/fava_catalog/) for our targets during the K2 observations.

6. Discussion

In Paper I we discussed the previous studies of AGNs made with Kepler and K2, and we refer to this for some details of that earlier work. Here we note two additional recent papers. Smith et al. (2018a, 2018b) analyzed 21 light curves of Type 1 AGNs that were measured by the original Kepler mission. They created individualized pixel maps and used two cotrending basis vectors for each. The PSD slopes of the two objects that were in common between their sample and our earlier Kepler program agreed within the errors. Aranzana et al. (2018) analyzed K2 long-cadence light curves of 252 AGNs of all types detected in Cycles 0–3, using the K2SFF light curves (the EVEREST light curves were not available when they began their work). For the one target that was both in their sample and ours, the BL Lac PKS B1130+008, we found very similar PSD slopes.

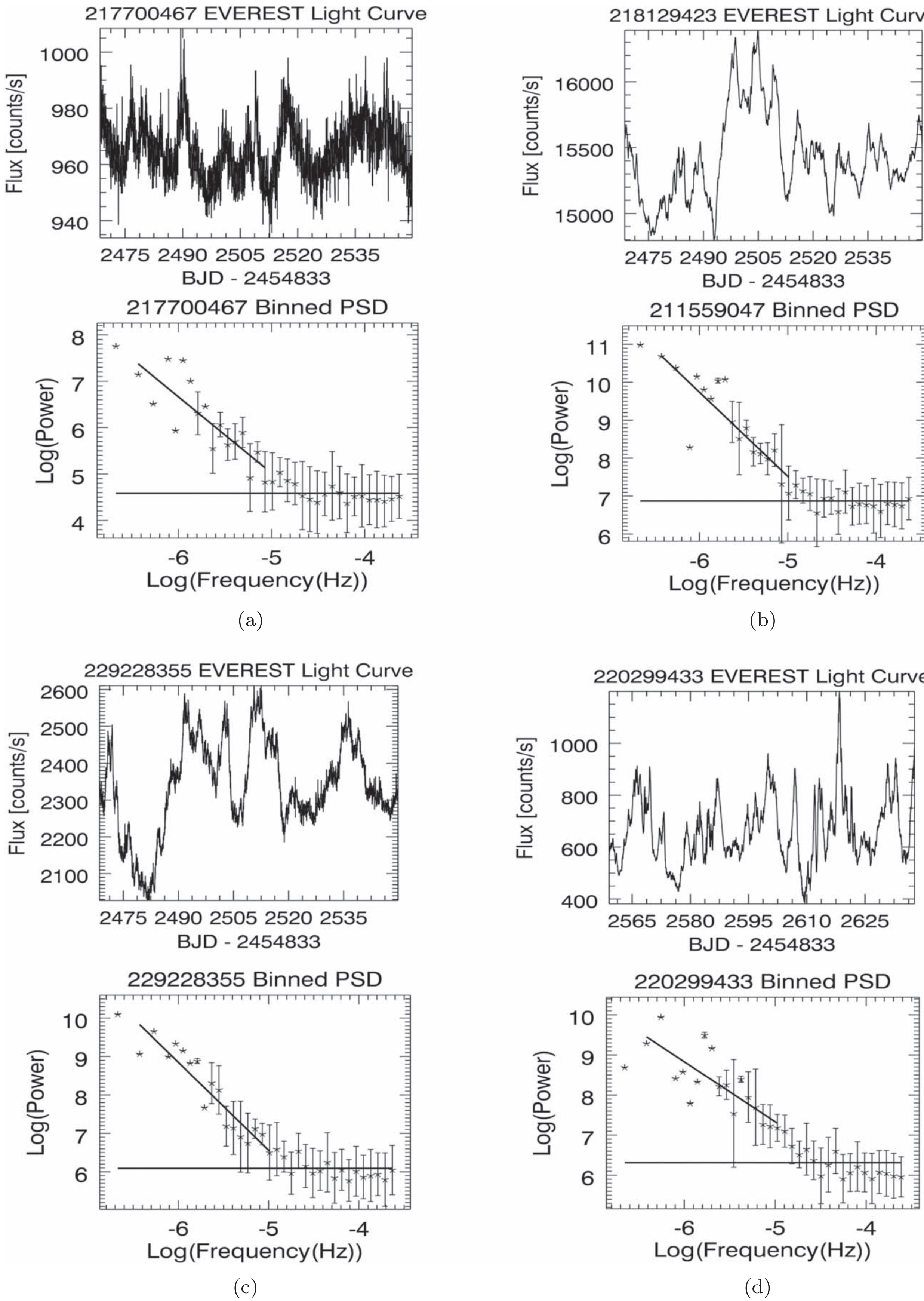

Figure 3. Long-cadence light curves as processed by EVEREST and binned power spectral densities. The targets are (a) EPIC 217700467 (also known as PKS B1908-201 and 3FGL J1911.2-2006), (b) EPIC 218129423 (also known as 1H 1914-194 and 3FGL J1917.7-1921), (c) EPIC 229228355 (also known as PKS B1921-293 and 3FGL J1924.8-2914), and (d) EPIC 220299433 (also known as PKS 0047+023 and 3FGL J0049.7+0237).

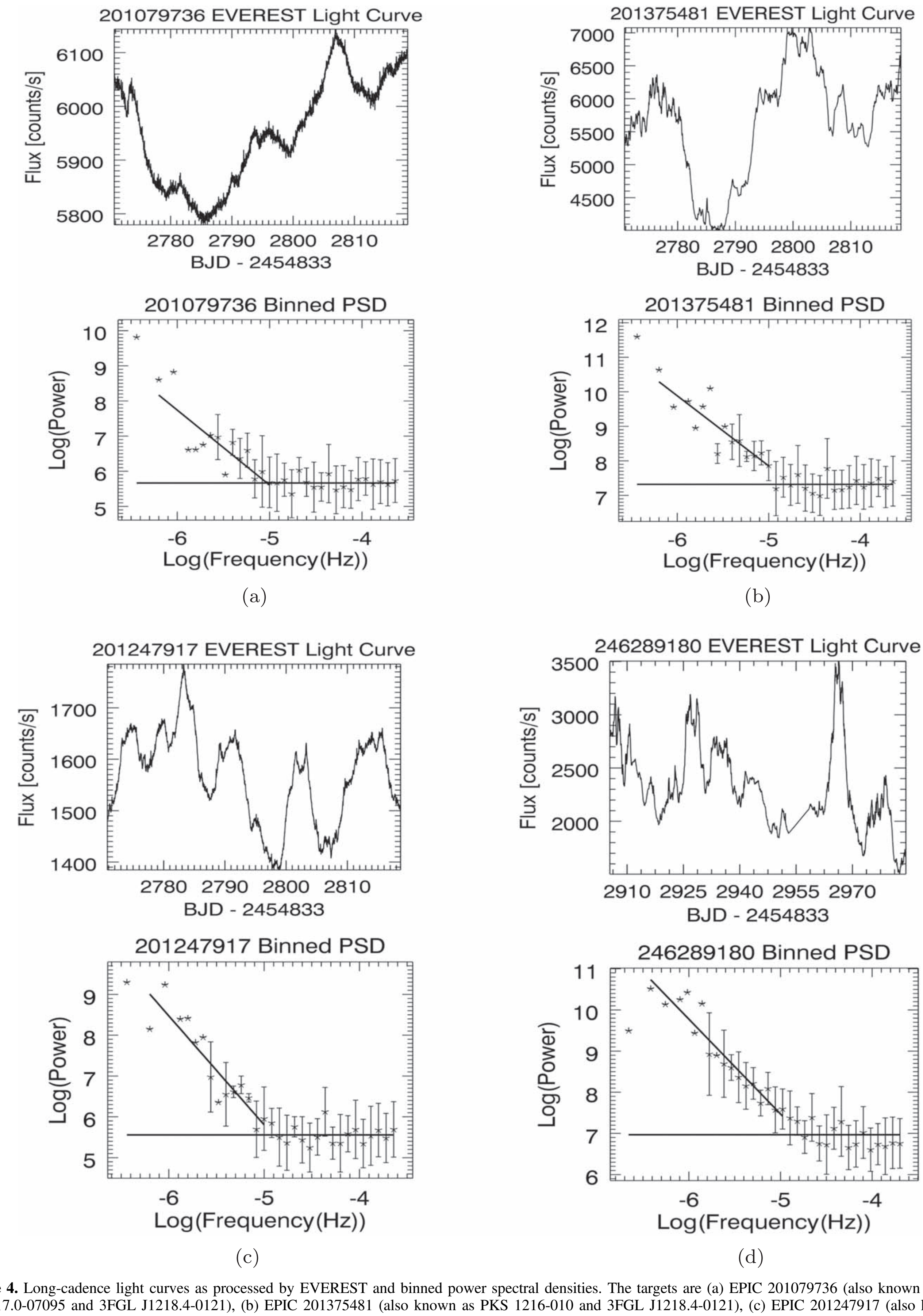

Figure 4. Long-cadence light curves as processed by EVEREST and binned power spectral densities. The targets are (a) EPIC 201079736 (also known as 1RXS J120417.0-07095 and 3FGL J1218.4-0121), (b) EPIC 201375481 (also known as PKS 1216-010 and 3FGL J1218.4-0121), (c) EPIC 201247917 (also known as 1RXS J121946.0-03141 and 3FGL J1219.7-0314), and (d) EPIC 246289180 (also known as PKS B2320-035 and 3FGL J2323.5-0315).

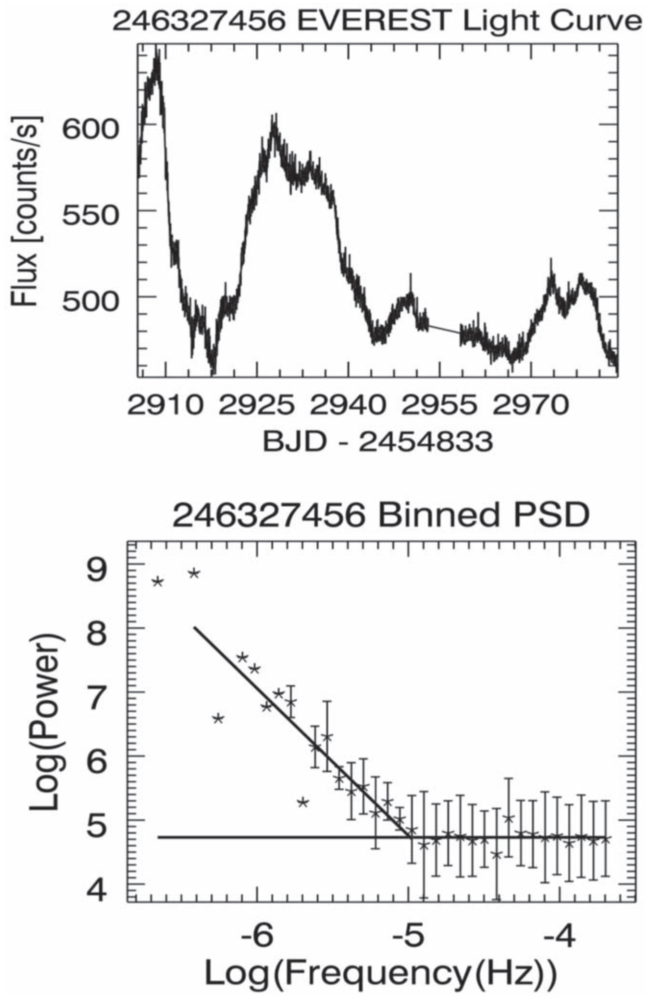

Figure 5. Long-cadence light curve as processed by EVEREST and binned power spectral densities. The target is EPIC 246327456 (also known as PKS B2335-027 and 3FGL J2338.1-0229).

6.1. 3C 273

6.1.1. Background on the Optical Emission

The optical spectrum of 3C 273 contains prominent emission lines within the K2 passband. In addition, its continuum emission rises toward the big blue bump, which peaks in the ultraviolet (see, e.g., Figure 1(a) in Shang et al. 2005). Both emission lines and continuum are variable (Schmidt & Smith 2000; Zhang et al. 2019). The optical continuum is dominated by thermal emission from the accretion disk during quiescent periods with a much smaller mini-blazar contribution from synchrotron emission originating in the relativistic jet (Impey et al. 1989; Smith et al. 1993). The nonthermal emission from the jet is much redder than the thermal emission (e.g., see the analyses by Zeng et al. 2018 and Zhang et al. 2019). Spectropolarimetry and photometry (V and R bands) during November 2008 through July 2018 were obtained by P. Smith at Steward Observatory in support of the Fermi mission http://james.as.arizona.edu/~psmith/Fermi/. The data were used by Zhang et al. (2019) for a reverberation-mapping campaign. The mean and rms spectra obtained by Zhang et al. (their Figure 2) showed that 3C 273 is more variable in the blue than in the red. Smith obtained one spectrum during K2 Campaign 10 in a gap in spacecraft data, on 2016 July 23 (Figure 8). It showed 3C 273 with its continuum rising to the blue, as was typical during his 10 years of monitoring. The entire optical spectral range (4000 to 7500 Å) of the Smith observation is encompassed by the broad Kepler passband; so the variability observed by K2 may come from anywhere or everywhere in the optical wave band.

As such a well-known quasar, 3C 273 has been very extensively studied, and here we mention only a few relevant recent papers. The optical variability of 3C 273 over periods ranging from minutes to over a decade (2005–2016) has recently been investigated by two groups using the same instruments (the Yunnan Astronomical Observatories 2.4 m and 1.02 m telescopes), albeit on different nights (27 nights in Xiong et al. 2017 and 108 nights in Zeng et al. 2018). During this lengthy period, the source was rather quiescent, with a total range of only about 0.7 mag (Xiong et al. 2017) and fractional amplitude variability of less than 0.5% (Zeng et al. 2018). Clear intraday variability of a few percent in flux was detected during around one-seventh of the nights for which sufficient data were gathered to make a proper search for it. On two nights, intraday variability of over 0.1 mag in just a few minutes may have been detected (Xiong et al. 2017), although these remarkable claims are based on only one or two differential light-curve points and so cannot be considered to be firmly established. The Yunnan telescope data did not have enough sampling at intervals similar to those of K2 to compare directly to our K2 data.

Recently, the Gravity Collaboration (2018) used near-infrared Very Large Telescope Interferometer observations to spatially resolve the Paschen-α emission line from 3C 273. They concluded that it arises from clouds in a thick-disk configuration of 150 light days in radius around a $2.6 \pm 1.1 \times 10^8$ $M_\odot$ black hole, which is consistent with, but somewhat lower than, most earlier reverberation-mapping mass estimates (e.g., Kaspi et al. 2000). Hence, any accretion disk component responsible for significant optical variations would have to be much smaller. The predominant optical-band-emitting region of a standard accretion disk of a quasar of 3C 273's luminosity around a supermassive black hole (SMBH) of that mass would be at a distance of a few light days, therefore, as elaborated upon below, variations on day-like timescales are consistent with a disk origin.

6.1.2. Structure of the 3C 273 PSD

K2 observed 3C 273 to vary by a factor of 1.02 over the course of the 49-day Campaign 10b(2). The short-cadence fit PSD slope was -2.77 ± 0.12 between log $\nu = -4$ to log $\nu = -6.2$, or timescales of 2.8 hours to 18.3 days. The slope was the steepest in the current sample, indicating that longer timescale red noise was relatively stronger, or alternatively, that shorter timescale fluctuations were relatively weaker, in this AGN than in the other targets when observed over comparable observer's time frames.

Case 1: The jet. The K2 variability of 3C 273 could have originated in the mini-blazar jet component for the following reasons. First, the fluctuations in the light curve appear similar in shape (symmetric rise and fall, sharply peaked profiles) to those of several other blazars in our sample that are almost certainly jet dominated. Second, the factor of 1.02 amplitude of the variations is consistent with the level of optical polarization and its variability. At least some of the variation must originate in polarized synchrotron emission (see polarization data online at http://james.as.arizona.edu/~psmith/Fermi/), probably

Table 3
Restricted Range Sweet-spot Slopes of Optical Power Spectral Densities

Name	EPIC ID	Average Count Rate (ct s^{-1})	SD[a] Count Rate (ct s^{-1})	Max/Min[b]	Slope	Error	PSRESP Slope	PSRESP Error	PSRESP Confidence %	Notes
PKS B1908-201	217700467	965	6	1.06	−1.65	0.31	−1.86	0.19	92	⋯
1H 1914-194	218129423	15424	28	1.11	−2.20	0.34	−2.20	0.18	36	⋯
PKS B1921-293	229228355	2337	14	1.29	−2.29	0.24	−2.24	0.19	77	⋯
PKS 0047+023	220299433	665	9	3.37	−1.49	0.31	−1.77	0.18	47	⋯
1RXS J120417.0-070959	201079736	5952	12	1.06	−2.14	0.42	−2.50	0.26	50	1
PKS 1216-010	201375481	5635	11	1.77	−2.01	0.33	−2.28	0.27	53	1, 2
3C 273	229151988	91737	18	1.02	−2.43	0.23	−2.48	0.30	52	1, 3
3C 273	229151988	91200	49	1.02	−2.55	0.34	⋯	⋯	⋯	1, 2, 4
3C 273	229151988	91200	49	1.02	−2.77	0.12	⋯	⋯	⋯	1, 4, 5
1RXS J121946.0-031419	201247917	1567	16	1.29	−2.67	0.36	−2.43	0.34	32	1
PKS B2320-035	246289180	2308	5	2.41	−2.35	0.19	−2.20	0.18	36	⋯
PKS B2335-027	246327456	511	3	1.43	−2.30	0.29	−2.45	0.23	31	⋯

Notes. 1. The first six days of Campaign 10 (when the spacecraft was mispointed) before the observation gap were omitted. 2. The sweet-spot fit frequency range was log $\nu = -5.0$ to -6.2. 3. This data set was long cadence. 4. This data set was short cadence. The short-cadence data set was too large for PSRESP to handle. 5. The fit frequency range was wider: log $\nu = -4.0$ to -6.2.
[a] Standard deviation during 0.2–0.5 day intervals when the source variation was less than ∼1%.
[b] (Maximum count rate)/(minimum count rate).

Doppler-boosted through relativistic beaming by only a modest amount due to its $9° \pm 2°$ inclination to the line of sight (Jorstad et al. 2017). If and when the majority of the optical flux comes from the accretion disk (and broad lines) contained within the broad K2 band, then larger variations of factors of 1.1 to 1.2 originating in the jet would appear as weak as those we observed. Third, models involving turbulence in a jet have produced PSD slopes in the rather broad range of −1.7 to −2.9 (Calafut & Wiita 2015; Pollack et al. 2016), encompassing that of 3C 273 and most of the other blazars in our sample. Fourth, fluctuations in the thermal emission from an accretion disk are unlikely to have a PSD slope steeper than −2, which is shallower than what we observed with K2. Both early generic phenomenological light-curve models for optical accretion disk variability (e.g., Mangalam & Wiita 1993; Xiong et al. 2000) and recent sophisticated ones involving high-resolution three-dimensional general relativistic magnetohydrodynamical simulations (e.g., Noble & Krolik 2009; Tchekhovskoy et al. 2011; O'Riordan et al. 2017; Curd & Narayan 2019), when they are analyzed to produce PSDs, find slopes between −1.2 and −2.2, at least for rotation axes that are oriented quite close to the observer's line of sight, as is the case for 3C 273. See Paper I for more details on the last two points. We conclude that a jet origin is plausible for the variations in the K2 light curve of 3C 273.

Case 2: The disk. On the other hand, the K2 variability of 3C 273 could have originated in a relatively small number of hot spots or clumps peppering the accretion disk. The small amplitude and sharply peaked shape of its individual hours-to-days fluctuations do look similar to those of three Seyfert 1 AGNs in the original Kepler field (KIC 9650712, KIC 12158940, and KIC 6932990 = Zw 229 − 15) studied by Smith et al. (2018a). For them, an accretion disk origin for optical variability is expected. Further, another one of those Seyferts, KIC 9650712, showed evidence for a quasi-periodic oscillation of ∼44 days and had a black hole mass they estimated from spectroscopy at $\sim 1.5 \times 10^8\ M_\odot$ (Smith et al. 2018b). For 3C 273, these small clumps would be a light day or so in diameter, orbiting on weeks-long timescales and probably growing and dying on similar timescales (e.g., Zhang & Bao 1991). These variable emitting clumps would be superimposed on larger and longer timescale optical variations that may originate from magneto-rotational instabilities in the accretion disk. At $\sim 2.6 \times 10^8\ M_\odot$, the black hole in 3C 273 is 25 to 100 times more massive than the black hole of a typical Seyfert 1. As the temperature of a standard Shakura & Sunyaev (1973) accretion disk scales essentially as $M_{\rm BH}^{-0.25}$ (and not very differently for other models), the optical emission from the 3C 273 accretion disk in its rest frame arises from closer (in terms of gravitational radii, $GM_{\rm BH}/c^2$) to the black hole than the optical emission from the accretion disk of a less massive black hole. However, the orbital period of clumps at the same distance (in gravitational radii) scales directly as the mass, so it is much longer for 3C 273 than for less massive Seyfert-type black holes. Multiplied together, the orbital and temperature-related mass dependency scales as the $M_{\rm BH}^{0.75}$. Consequently, the brightness changes due to overall changes in conditions in the full accretion disk take substantially longer to rise and fall in 3C 273 than in most Seyfert 1 nuclei, by roughly a factor of $(3 \times 10^8/10^7)^{0.75}$ or ∼13. Hence we conclude that hot spots or clumps in the accretion disk, but not changes in the overall full disk, are plausible for the origin of the variations in the K2 light curve of 3C 273.

6.2. Results on Other Individual AGNs

We present our results on the other nine individual AGNs as follows. Light curves and binned PSDs are shown in Figures 3–5. The figures are time-ordered by K2 Campaign number (listed in Table 1) to allow easy identification of common instrumental effects, as described in Paper I.

PKS B1908−201 = EPIC 217700467: This is an FSRQ at redshift 1.12 with $K_p = 16.471$. It was clearly detected (TS = 68.7) by Fermi-LAT during our K2 observations. The K2 light curve optical maximum to minimum ratio was 1.06 with a noisy spiky structure. Its PSD slope was measured to be -1.65 ± 0.31 and the PSRESP slope was consistent at

Table 4
Restricted Range Sweet-spot Slopes of Optical Power Spectral Densities of Paper I Targets

Name	EPIC ID	Average Count Rate (ct s^{-1})	SD[a] Count Rate (ct s^{-1})	Max/Min[b]	Slope	Error	PSRESP Slope	PSRESP Error	PSRESP Confidence %	Notes
PKS B1130+008	201503438	884	3.3	1.22	−2.48	0.23	−2.03	0.21	29	…
WB J0905+1358	211559047	1908	3	1.59	−2.12	0.30	−2.52	0.36	47	1
3C 207	211504760	589	5	1.32	−1.96	0.21	−2.06	0.29	95	…
RGB J0847+115	211394951	1800	4.8	1.44	−2.09	0.37	−2.39	0.29	68	2
OJ 287	211991001	17001	18,47	2.8	−2.25	0.22	−2.33	0.26	53	3
PKS 1329-049	229227170	310	2.3	1.14	−1.54	0.23	−1.78	0.16	32	4
RBS 1273	212800574	11738	4.5	1.03	−1.14	0.32	−1.78	0.27	19	5
PKS 1335-127	212489625	1204	2.2	2.23	−2.55	0.22	−2.10	0.22	35	…
PKS 1352-104	212595811	2418	3.9	6.24	−2.01	0.24	−2.40	0.37	50	6

Notes. Some table notes are repeated verbatim from Paper I for completeness. 1. EPIC 211559047 (WB J0905+1358): The target is on the edge of the extraction aperture used by EVEREST, as a result, the EVEREST data were noisy. We used the less noisy K2SFF data in our PSDs for this target. 2. EPIC 211394951 (RGB J0847+115): No EVEREST data were available. We used K2SFF data for this target. 3. EPIC 211991001 (OJ 287): This data set was long cadence. 4. EPIC 229227170 (PKS 1329-049): The target has the noisiest light curve in our sample, which may contribute to the discrepancy between the slopes. 5. EPIC 212800574 (RBS 1273): We included data starting at day 2389. 6. EPIC 212595811 (PKS 1352-104): Data set included the big flare. PSRESP was not fit independently for this log ν interval.

[a] Standard deviation during 0.2–0.5 day intervals when the source variation was less than ∼1%; for OJ 287 there were only two such intervals.

[b] (Maximum count rate)/(minimum count rate).

-1.86 ± 0.19, with a 92% confidence level. This bright radio source has often been used for calibration of radio telescopes. It has been observed with VLBI beginning in the early 1980s (Wehrle et al. 1984), more recently as part of the MOJAVE survey (e.g., Lister et al. 2016), and with the space VLBI mission VSOP (e.g., Dodson et al. 2008). Superluminal motion at 4.4 ± 1.2 c was reported by Lister et al. (2019). It was detected by *CGRO*–EGRET (e.g., Hartman et al. 1999) and later by Fermi-LAT (e.g., Acero et al. 2015). It has not been the subject of a dedicated paper.

1H 1914−194 = EPIC 218129423: This is a BL Lac object at redshift 0.137 with $K_p = 15.341$. It was detected (TS = 32.5) by Fermi-LAT during our K2 observations. The K2 light curve optical maximum to minimum ratio was 1.11 with a well-defined series of peaks and valleys. Its PSD slope was measured to be -2.20 ± 0.34 and the PSRESP slope was identical at -2.20 ± 0.18, with a 36% confidence level. Examination of the light curve in 5-day chunks showed credible rises and falls on timescales of a few hours, hence, the source may be displaying fractal variability well beyond the sweet-spot cutoff of 1.1 days or log $\nu = -5.0$. It was detected in early X-ray (Wood et al. 1984) and radio (Large et al. 1981) surveys. It has a host galaxy that was detected but not resolved by the Hubble Space Telescope (Urry et al. 2000). Nuclear emission lines as well as absorption lines from the host galaxy at a redshift of 0.137 were detected by Carangelo et al. (2003).

PKS B1921−293 = EPIC 229228355, also known as OV-236: This is a BL Lac object at redshift 0.353 with $K_p = 16.410$. It was not detected (upper limit of 3.75×10^{-8} ph s^{-1} cm^{-2}) by Fermi-LAT during our K2 observations. The K2 light curve optical maximum to minimum ratio was 1.29. Its PSD slope was measured to be -2.29 ± 0.24 and the PSRESP slope was completely consistent at -2.24 ± 0.19, with a 77% confidence level. This source also displayed credible rises and falls on timescales of a few hours when the light curve was examined in 5-day chunks, hence, the source may also be displaying fractal variability well beyond the sweet-spot cutoff of 1.1 days or log $\nu = -5.0$. This well-studied BL Lac object was briefly the brightest object in the radio sky at centimeter bands (Dent & Balonek 1980). Following many years of VLBI observations in various surveys, it was the first AGN imaged with VLBI at 230 GHz, demonstrating the feasibility of the Event Horizon Telescope (Lu et al. 2012). Superluminal motion of 6.96 ± 0.92 c was reported by Lister et al. (2019).

PKS 0047+023 = EPIC 220299433: This is a faint ($K_p = 18.84$) BL Lac object whose redshift lower limit (0.55) was estimated from the nondetection of starlight by Paiano et al. (2017), see their discussion of its featureless spectrum. An earlier redshift estimate of 1.44 (Rau et al. 2012) listed in the SDSS catalog was based on multiband photometry, which is not a reliable technique for objects whose optical emission is synchrotron dominated. It was clearly detected (TS = 45.5) by Fermi-LAT during our K2 observations. The K2 light curve optical maximum to minimum ratio was 3.37. Its K2 optical light curve is the spikiest in our sample and has the flattest PSD slope in our sample, -1.49 ± 0.31. As with PKS B1921−293 and 1H 1914−194, we find credible rises and falls on timescales of a few hours when the light curve is examined in 5-day chunks, hence, the source may be displaying fractal variability well beyond the sweet-spot cutoff of 1.1 days or log $\nu = -5.0$. The PSRESP slope was consistent, at -1.77 ± 0.18, with a 47% confidence level. Like many of our targets, it has been extensively studied with the VLBI.

1RXS J120417−070959 = EPIC 201079736: This is an X-ray selected BL Lac object ($K_p = 16.305$, redshift = 0.184) with a host galaxy clearly visible in digitized POSS images. It was not detected (upper limit of 2.98×10^{-8} ph s^{-1} cm^{-2}) by Fermi-LAT during our K2 observations. The K2 light curve optical maximum to minimum ratio was 1.06 with three peaks in a slowly varying structure. Its PSD slope was measured to be -2.14 ± 0.42 and the PSRESP slope was consistent within the errors at -2.50 ± 0.26, with a 50% confidence level. Although a member of many radio, infrared, optical, and X-ray survey samples, it has not been the subject of a dedicated paper.

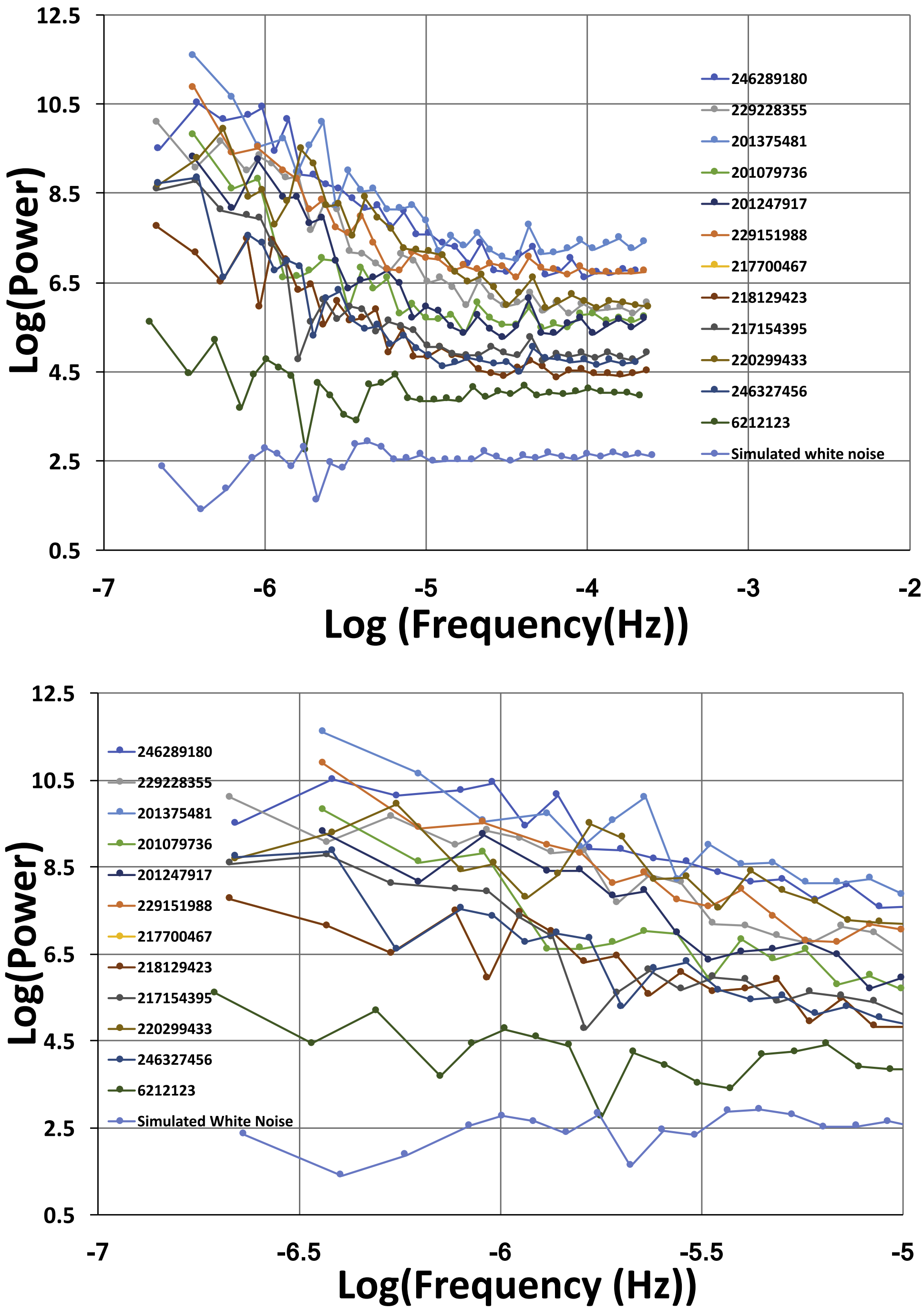

Figure 6. Top: PSDs of the 10 K2 AGN targets, the white dwarf target KIC 6212123 observed during the Kepler mission, and simulated white noise, unbinned in log ν, shown over the full frequency range. White noise dominated the PSDs from log $\nu = -3.6$ to approximately log $\nu = -5.0$. Red noise dominated the PSDs over the rest of the frequency range. The AGN PSDs are noticeably steeper (redder) than the white dwarf PSD whose shallow red-noise slope is probably mostly residual instrumental noise. Bottom: The PSDs of the 10 AGN targets, the white dwarf target KIC 6212123, and simulated white noise, unbinned in log ν, shown over the sweet-spot frequency range. The sweet spot was defined as the frequency range between the transition from white noise to red noise and the Nyquist-sampled frequency for each campaign length. PSD slopes were fit to the sweet-spot range.

PKS 1216−010 = EPIC 201375481: This is a highly polarized BL Lac object (e.g., Sluse et al. 2005) at redshift 0.415 with $K_p = 16.626$. It was not detected (upper limit of 2.82×10^{-8} ph s^{-1} cm^{-2}) by Fermi-LAT during our K2 observations. The K2 light curve optical maximum to minimum ratio was 1.77. Its PSD slope was measured to be -2.01 ± 0.33 and the PSRESP slope was consistent at -2.28 ± 0.27, with a 53% confidence level. This object is another example of a source that may be displaying fractal variability well beyond the sweet-spot cutoff of 1.1 days or log $\nu = -5.0$, as examination of the light curve in 5-day chunks showed credible rises and falls on timescales of a few hours. Observations of this source were undertaken to search for intranight optical variability by Sagar et al. (2004), who found that it faded by 0.11 mag and brightened by 0.14 mag over the course of a few days.

1RXS J121946.0−031419 = EPIC 201247917: This X-ray and radio-selected object (Bauer et al. 2000) was confirmed as

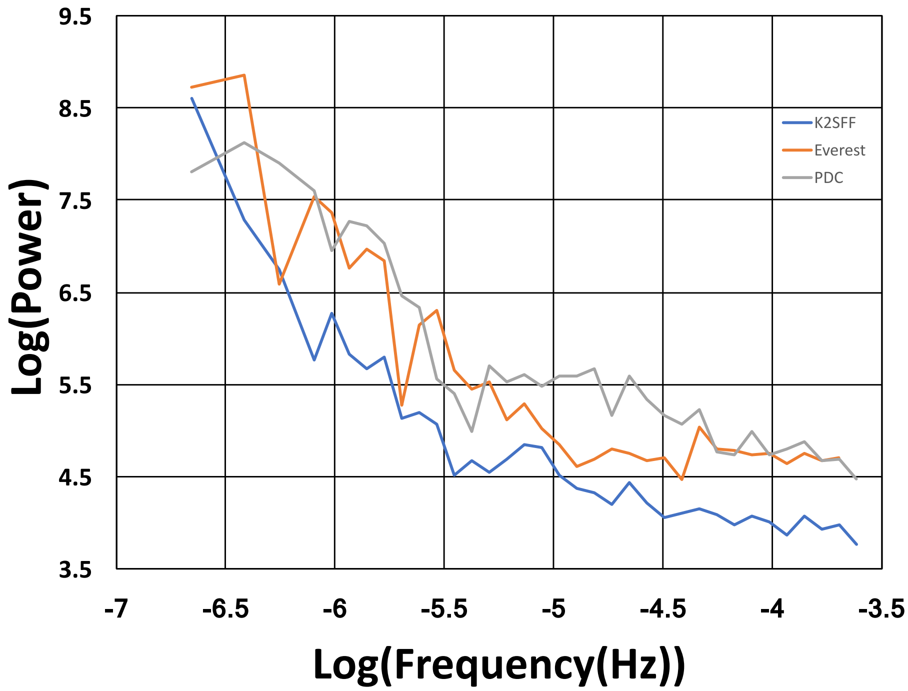

Figure 7. Comparison of PSDs resulting from three light-curve processing methods of EPIC 246327456, also known as PKS B2335-027: PDC (gray), EVEREST (orange), and K2SFF (blue). The PDC, EVEREST, and K2SFF methods yielded sweet-spot slopes of -2.14 ± 0.24, -2.30 ± 0.29, and -1.70 ± 0.19, respectively. The slopes for a more restricted range of log $\nu = -5.5$ to -6.4 were in closer agreement: -2.80 ± 0.32, -2.59 ± 0.64, and -2.52 ± 0.25, respectively.

a BL Lac using spectroscopic observations in the SDSS (Collinge et al. 2005). It has a redshift of 0.299 and $K_p = 17.091$. It was not detected (upper limit of 2.82×10^{-8} ph s^{-1} cm^{-2}) by Fermi-LAT during our K2 observations. The K2 light curve optical maximum to minimum ratio was 1.29 with six peaks of several days duration each. Its PSD slope was measured to be -2.67 ± 0.36 and the PSRESP slope was consistent at -2.43 ± 0.34, with a 36% confidence level. The light curve showed credible rises and falls on timescales of a few hours when examined in chunks of 5 days, hence, the source may be displaying fractal variability well beyond the sweet-spot cutoff of 1.1 days or log $\nu = -5.0$. It is often used as a member of various BL Lac samples, but it has not been the subject of individual analysis.

PKS B2320−035 = EPIC 246289180: This is an FSRQ with the highest redshift (1.41) in our sample and $K_p = 18.362$. It was strongly detected (TS = 251.6) by Fermi-LAT during our K2 observations. The K2 light curve optical maximum to minimum ratio was 2.41 with a spiky structure. Its PSD slope was measured to be -2.35 ± 0.19 and the PSRESP slope was consistent at -2.20 ± 0.18, with a 36% confidence level. As with five other objects in this paper, examination of the light curve in 5-day chunks showed credible rises and falls on timescales of a few hours, hence the source may be displaying fractal variability well beyond the sweet-spot cutoff of 1.1 days or log $\nu = -5.0$. This well-studied bright radio quasar was detected by both EGRET and COMPTEL on the *Compton Gamma Ray Observatory* (Hartman et al. 1999; Schonfelder et al. 2000 and references therein.) Romero et al. (2002) did not detect microvariability over the course of two nights in 2001 (V mag = 16.61 ± 0.02 and 16.58 ± 0.02).

PKS B2335−027 = EPIC 246327456: This is an optically faint, radio-bright quasar with $K_p = 18.318$ and redshift 1.072. It was detected (TS = 34.3) by Fermi-LAT during our K2 observations. The K2 light curve optical maximum to minimum ratio was 1.43 with four peaks of several days duration each. Its PSD slope was measured to be -2.30 ± 0.29 and the PSRESP slope was consistent at -2.45 ± 0.23, with a 31% confidence level. As with many of our K2 targets, it is used in the International Celestial Reference Frame (e.g., Fey et al. 2004) and is a calibrator for various radio interferometers.

6.3. Ensemble Results

6.3.1. Slopes of Optical Power Spectral Densities

The slopes of the optical PSDs of the 10 new long-cadence light curves over the sweet-spot red-noise frequency ranges (generally from log ν ranging from -5.0 to -6.2) vary from -1.49 ± 0.31 to -2.67 ± 0.36 (Table 3). The sweet-spot slopes for the nine targets in Paper I range from -1.14 ± 0.32 to -2.55 ± 0.22 (Table 4). We show a combined histogram of PSD slopes in Figure 9 in the sweet spot for targets in both this paper and Paper I. Inspection of Figure 9 indicates that 15 of the 19 slopes are different from the asymptotic -2 slope of the damped random walk model explored by Kelly et al. (2009). However, this could be a function of the choice of binning for the figure. Considering the slopes and their uncertainties, we find that the slopes of nine sources differ from a slope of -2.0 by at least 1σ and the slopes of five sources differ from -2.0 by 2σ or more. Four optical PSD slopes are flatter, and eleven slopes are steeper than -2, including 3C 273. As described earlier, we and others found slopes steeper than -2 for three FSRQs and a Seyfert 1.5 (Wehrle et al. 2013; Revalski et al. 2014). Mushotzky et al. (2011), Kasliwal et al. (2015), and Smith et al. (2018a, 2018b) found some significantly steeper slopes for various AGNs observed with Kepler in its original observing mode.

The application of continuous-time autoregressive moving average (CARMA) models (e.g., Kelly et al. 2009, 2014) to light curves plausibly assume that a light curve is a realization

Table 5
Fermi-LAT Results

Name	EPIC ID	Fermi Source Name	γ-ray Flux[a] ph s^{-1} cm^{-2}	γ-ray Flux Error[a] ph s^{-1} cm^{-2}	Test Statistic[a]	3FGL γ-ray Flux[b] ph s^{-1} cm^{-2}	3FGL γ-ray Flux Error[b] ph s^{-1} cm^{-2}	3FGL Detection Significance σ
PKS B1908-201	217700467	3FGL J1911.2-2006	6.29 E-8	9.93 E-9	68.7	3.72E-09	1.93E-10	32.1
1H 1914-194	218129423	3FGL J1917.7-1921	1.11 E-8	3.53 E-9	32.5	2.89E-09	1.73E-10	28.8
PKS B1921-293	229228355	3FGL J1924.8-2914	<3.75 E-8	…	…	2.16E-09	1.50E-10	27.4
PKS 0047+023	220299433	3FGL J0049.7+0237	1.67 E-8	5.96 E-9	45.5	7.90E-10	9.30E-11	13.1
1RXS J120417.0-07095	201079736	3FGL J1204.3-0708	<2.98 E-8	…	…	1.05E-09	1.11E-10	15.8
PKS 1216-010	201375481	3FGL J1218.4-0121	<2.82 E-8	…	…	1.12E-09	1.17E-10	13.8
3C 273	229151988	3FGL J1229.1+0202	1.24 E-7	1.92 E-8	93.5	9.42E-09	2.53E-10	149.0
1RXS J121946.0-03141	201247917	3FGL J1219.7-0314	<2.50 E-8	…	…	5.72E-10	9.15E-11	8.7
PKS B2320-035	246289180	3FGL J2323.5-0315	7.29 E-8	9.25 E-9	251.6	3.03E-09	1.60E-10	39.3
PKS B2335-027	246327456	3FGL J2338.1-0229	1.98 E-8	6.03 E-9	34.3	1.27E-09	1.13E-10	19.0

Notes.
[a] Fluxes and test statistics were in the energy range 0.1-500 GeV, upper limits were in the energy range 0.1–300 GeV, measured during K2 campaigns in 2015-2017.
[b] Data obtained from the Fermi-LAT Third Source Catalog (3FGL, Acero et al. 2015), in the energy range 1–100 GeV, observed between 2008 August 4 and 2012 July 31, retrieved from https://fermi.gsfc.nasa.gov/ssc/data/.

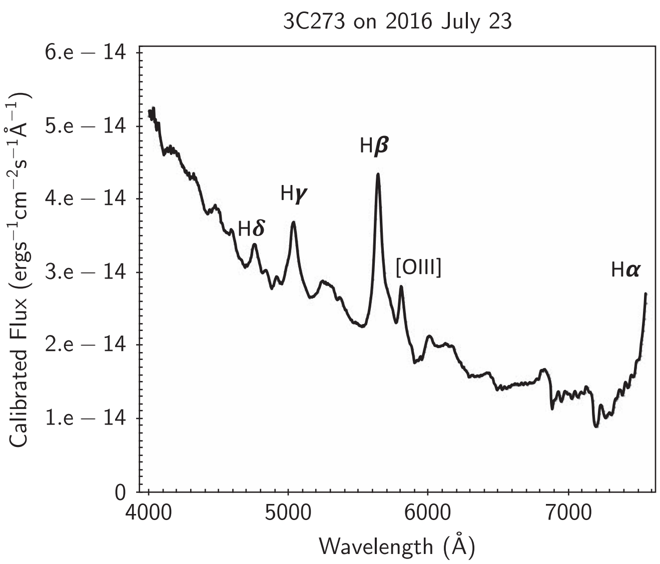

Figure 8. An optical spectrum of 3C 273 obtained by P. Smith at Steward Observatory on 2016 July 23 during K2 Campaign 10, but in a gap in spacecraft data. Variability in the K2 data may come from anywhere in the optical wave band. The spectrum has not been corrected for Galactic reddening or absorption. Prominent emission lines include Hδ, Hγ, Hβ, and [OIII], with part of the Hα line just visible at the red end of the spectrum. The spectrum retains the atmospheric O_2 B-band absorption feature at about 6980 Å. The data were downloaded from http://james.as.arizona.edu/~psmith/Fermi/.

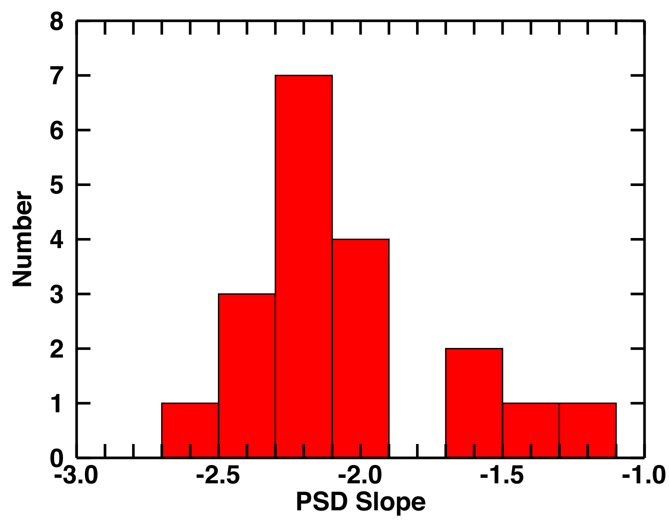

Figure 9. Histogram of PSD slopes of the long-cadence light curves, determined in the sweet-spot frequency range via the discreet Fourier transform. We find that the slopes of nine sources differ from a slope of -2.0 by at least 1σ and the slopes of five sources differ from -2.0 by 2σ or more.

of a Gaussian noise process. CARMA(p, q) models connect the light curve and its first p time derivatives to the noise and its first q time derivatives (see Kelly et al. 2014, their Equation (1) and following text for definitions). They generalize the damped random walk (also known as CAR(1) model, CARMA(1,0) model, or an Ornstein-Uhlenbeck process). This is effectively a Green function approach to use variability to measure the timescales of perturbations and characterize the driving flux perturbations (Kasliwal et al. 2017). Physically, the AR aspect of CARMA corresponds to short-term memory, while the MA piece governs the amplitude of random perturbations at different timescales. Together, AR and MA reconstruct the correlation structure and degree of smoothness of noisy processes (Moreno et al. 2019). The generalized models can allow for some steeper PSD slopes than the damped random walk and also can provide a way to more precisely identify any breaks (or even multiple breaks) in PSDs, although care must be taken to avoid artificial PSD breaks when using this approach (Ryan et al. 2019). It appears that while the CARMA (1,0) models frequently do not adequately describe the variability properties of blazar γ-ray light curves, the modestly more complex CARMA(2,1) models usually do so (Ryan et al. 2019). They indicate the presence of PSD break timescales on the order of one year for 4 of 13 blazars recently studied by Ryan et al. (2019), which they argue likely represent a thermal or dynamical timescale in the accretion disk; whereas the one break seen around 8–9 days (Nakagawa & Mori 2013) in 3C 454.3 can be fit using a CARMA(3,2) model and more likely arises from the jet (Ryan et al. 2019). Application and results of CARMA modeling to our objects is beyond the scope of this paper, but will be addressed in a future publication.

Given that these are all bona fide blazars where jet contributions are strong, we would expect that most of these observed optical variations arise in the Doppler-boosted jet. The fairly substantial, but not extreme (i.e., much steeper than -2.5 or shallower than -1.5) range of measured PSD slopes for this combined sample of 19 can be produced by turbulent jet models (e.g., Pollack et al. 2016). However, as it appears to be more difficult to produce the observed range of slopes from accretion disk models, we favor a jet origin for the observed variations in this combined sample; see Paper I for more details on this point.

6.3.2. γ-ray Activity Level and Blazar Classes

A systematic correlation between the γ-ray and optical fluxes in 15 out of 24 blazars (including some with nonzero time lags) in 2008–2014 was found by Itoh et al. (2016), see their Figures 4 and 5 and their Table 5. They also showed that significant correlations between the γ-ray and optical variability with both γ-ray and the optical luminosities appeared to be present on weekly and longer timescales. These optical light curves contained a few tens to several hundred points over six years; hence, the sampling was not comparable to that obtained with K2. We note that Howard et al. (2004) have previously suggested that optical microvariabilty on timescales of minutes to hours may be correlated with changes in brightness rather than optical brightness itself, but there are very little γ-ray data available on such brief intervals. We looked for suggestions of a relationship between γ-ray detection during our K2 observations and optical variability amplitude. Six of the 10 AGNs were detected with Fermi-LAT at significance levels $\gtrsim 5\sigma$ (TS $\gtrsim 25$) during the K2 observations. We note that three of the four nondetections occurred in Campaign 10, which was much shorter than the other campaigns; if Campaign 10 had been longer, the three targets may have had a better chance of being detected.

The K2-measured optical variability amplitude (ratio of maximum to minimum count rate) was higher for the AGNs detected with the Fermi-LAT during the K2 observations than for the nondetected AGNs in both the current sample and in the Paper I sample. Specifically, the maximum to minimum ratios for γ-ray detected versus nondetected AGNs were 1.02–3.37 versus 1.06–1.77 for the current sample and 1.22–6.24 versus 1.03–1.32 for the Paper I sample. However, none of the sources detected with Fermi-LAT at significance levels $\gtrsim 5\sigma$ (TS $\gtrsim 25$) were found to be in an enhanced γ-ray activity state when we examined the light curves in the 4FGL Catalog (Abdollahi et al. 2020). The slopes of the optical power spectral densities of the four blazars not contemporaneously detected by the Fermi-LAT spanned a broad range (-2.01 ± 0.33 to -2.67 ± 0.36), as did those of the detected-contemporaneously blazars (-1.49 ± 0.31 to -2.43 ± 0.23). The PSD slopes of the six BL Lac objects and four FSRQs spanned similar ranges and had similar average values. Similar results were found for the original PSD slopes of BL Lacs and FSRQs in Paper I and for the Paper I targets refit with sweet-spot frequency ranges as discussed here. Both results are consistent with the relativistic jet acting as the dominant source of emission in both types of objects during the K2 observations.

7. Summary

Our main results are as follows:

1. 3C 273 was quiescent during the K2 observations, varying by only a factor of 1.02. Its light curve and PSD are consistent with both thermal emission from hot spots in the disk and with turbulence in nonthermal synchrotron emission from the relativistic jet.

2. 3C 273 and OJ 287 have similar PSD slopes, the reddest in our sample, even though 3C 273 varied by only a factor of 1.02 and OJ 287 by a factor of 2.8. 3C 273 may have acted like a buried mini-blazar embedded in much stronger disk emission, while OJ 287 behaved like a strong blazar.

3. Of the nine other AGNs we observed, three objects, PKS 0047+023, PKS 1216-10, and PKS B2320-035, were active, varying by factors of 1.8–3.4. Three objects varied by factors of 1.1–1.4. The three remaining objects were comparatively quiet, varying by factors of less than 1.1. Of the six most variable sources, five have light curves with PSDs that are not consistent with damped random walks. All six have light curves and PSDs consistent with the variable emission observed by K2 originating in turbulent relativistic jets and not with hot spots in the disk emission. As discussed in Paper I, mechanisms operating in the jet other than turbulence, such as mini-jets or "jet-in-jets" (e.g., Giannios et al. 2009), may also produce the observed range of PSD slopes.

4. Six of the 10 AGNs were detected with Fermi-LAT at significance levels $\gtrsim 5\sigma$ (TS $\gtrsim$ 25) during the K2 observations. None of these sources was found to be in an enhanced γ-ray activity state during the K2 observations.

We thank the referee for a careful reading of the manuscript and useful suggestions. We are grateful to Rodrigo Luger (University of Washington and Flatiron Institute) for advice on processing the 3C 273 short-cadence data through EVEREST software. We thank Paul Smith (Steward Observatory) for helpful discussions and for optical spectrophotometry of 3C 273. We acknowledge NASA K2 Guest Investigator Program support via NNX16AI61G and 80NSSC17K0201. This paper includes data collected by the K2 mission. Funding for the K2 mission is provided by the NASA Science Mission Directorate.

The Fermi-LAT Collaboration acknowledges generous ongoing support from a number of agencies and institutes that have supported both the development and the operation of the LAT as well as scientific data analysis. These include the National Aeronautics and Space Administration and the Department of Energy in the United States, the Commissariatl' Energie Atomique and the Centre National de la Recherche Scientifique/Institut National de Physique Nucléaire et de Physique des Particules in France, the Agenzia Spaziale Italiana and the Istituto Nazionale di Fisica Nucleare in Italy, the Ministry of Education, Culture, Sports, Science and Technology (MEXT), High Energy Accelerator Research Organization (KEK) and Japan Aerospace Exploration Agency (JAXA) in Japan, and the K.A. Wallenberg Foundation, the Swedish Research Council and the Swedish National Space Board in Sweden. Additional support for science analysis during the operations phase is gratefully acknowledged from the Istituto Nazionale di Astrofisica in Italy and the Centre National d' Études Spatiales in France. This work performed in part under DOE Contract DE- AC02-76SF00515.

This research has made use of the NASA/IPAC Extragalactic Database (NED) which is operated by the Jet Propulsion Laboratory, California Institute of Technology, under contract with the National Aeronautics and Space

Administration. Some of the data presented in this paper were obtained from the Mikulski Archive for Space Telescopes (MAST). STScI is operated by the Association of Universities for Research in Astronomy, Inc., under NASA contract NAS5-26555. Support for MAST for non-HST data is provided by the NASA Office of Space Science via grant NNX09AF08G and by other grants and contracts.

Facility: Kepler, K2, Fermi.

Software: EVEREST (Luger et al. 2016), K2SFF (Vanderburg & Johnson 2014).

ORCID iDs

Michael Carini https://orcid.org/0000-0001-8961-2465
Ann E. Wehrle https://orcid.org/0000-0003-4737-1477
Paul J. Wiita https://orcid.org/0000-0002-1029-3746

References

Abdollahi, S., Acero, F., Ackermann, M., et al. 2020, ApJS, 247, 33
Abdollahi, S., Ackermann, M., Ajello, M., et al. 2017, ApJ, 846, 34
Acero, F., Ackermann, M., Ajello, M., et al. 2015, ApJS, 218, 23
Ackermann, M., Ajello, M., Allafort, A., et al. 2011, ApJ, 743, 171
Aranzana, E., Koerding, E., Uttley, P., Scaringi, S., & Bloemen, S. 2018, MNRAS, 481, 2140
Atwood, W. B., Baldini, L., Bregeon, J., et al. 2013, ApJ, 774, 76
Bauer, F. E., Condon, J. J., Thuan, T. X., & Broderick, J. J. 2000, ApJS, 129, 547
Calafut, V., & Wiita, P. J. 2015, JApA, 36, 255
Carangelo, N., Falomo, R., Kotilainen, J., Treves, A., & Ulrich, M.-H. 2003, A&A, 412, 651
Chidiac, C., Rani, B., Krichbaum, T. P., et al. 2016, A&A, 590, A61
Collinge, J. J., Strauss, M. A., Hall, P. B., et al. 2005, AJ, 129, 2542
Curd, B., & Narayan, R. 2019, MNRAS, 483, 565
Dent, W., & Balonek, T. 1980, Natur, 283, 747
Dodson, R., Fomalont, E. B., Wiik, K., et al. 2008, ApJS, 175, 314
Doyle, T. F., Howell, S. B., Petit, V., & L'epine, S. 2017, MNRAS, 464, 3464
Fernandes, S., Patiño-Álvarez, V. M., Chavushyan, V., Schlegel, E. M., & Valdés, J. R. 2020, MNRAS, 497, 2066
Fey, A. L., Ma, C., Arias, E. F., et al. 2004, AJ, 127, 3587
Giannios, D., Uzdensky, D. A., & Begelman, M. C. 2009, MNRAS, 395, L29
Gravity Collaboration, A. 2018, Natur, 563, 657
Hartman, R. C., Bertsch, D. L., Bloom, S. D., et al. 1999, ApJS, 199, 79
Högbom, J. A. 1974, A&AS, 15, 417
Howard, E., Webb, J. R., Pollock, J. T., et al. 2004, AJ, 127, 17
Huber, D., & Bryson, S. T. 2018, KSCI-19082-06 (Moffet Field, CA: NASA Ames Research Center)
Huber, D., Bryson, S. T., Haas, M. R., et al. 2016, ApJS, 224, 2
Impey, C. D., Malkan, M. A., & Tapia, S. 1989, ApJ, 347, 96
Itoh, R., Nalewajko, K., Fukazawa, Y., et al. 2016, ApJ, 833, 771
Jorstad, S. G., Marscher, A. P., Morzova, D. A., et al. 2017, ApJ, 846, 78
Kasliwal, V. P., Vogeley, M. S., & Richards, G. T. 2017, MNRAS, 470, 3027
Kasliwal, V. P., Vogeley, M. S., & Richards, G. T. 2015, MNRAS, 451, 4328
Kaspi, S., Smith, P. S., Netzer, H., et al. 2000, ApJ, 533, 631
Kelly, B. C., Bechtold, J., & Siemiginowska, A. 2009, ApJ, 698, 895
Kelly, B. C., Becker, A. C., Sobolewska, M., Siemiginowska, A., & Uttley, P. 2014, ApJ, 788, 33
Kolodziejczak, J. J., Caldwell, D. A., Van Cleve, J. E., et al. 2010, Proc. SPIE, 7742, 77421G
Large, M. I., Mills, B. Y., Little, A. G., Crawford, D. F., & Sutton, J. M. 1981, MNRAS, 194, 693
Li, Y.-R., Zhang, Z.-X., Jin, C., et al. 2020, ApJ, 897, 18
Lister, M., Aller, M. F., Aller, H. D., et al. 2016, AJ, 152, 12
Lister, M. L., Homan, D. C., Hovatta, T., et al. 2019, ApJ, 874, 43
Lu, R.-S., Fish, V. L., Weintroub, J., et al. 2012, ApJL, 757, 14
Luger, R., Agol, R., Kruse, E., et al. 2016, AJ, 152, 100
Luger, R., Kruse, E., Foreman-MacKay, D., Agol, E., & Saunders, N. 2018, AJ, 156, 99
Mangalam, A. V., & Wiita, P. J. 1993, ApJ, 406, 420
Moreno, J., Vogeley, M., Richards, G. T., et al. 2019, PASP, 131, 063001
Mushotzky, R. F., Edelson, R., Baumgartner, W., & Gandhi, P. 2011, ApJL, 743, L12
Nakagawa, K., & Mori, M. 2013, ApJ, 773, 177
Noble, S. C., & Krolik, J. H. 2009, ApJ, 703, 964
O'Riordan, M., PeÕer, A., & McKinney, J. C. 2017, ApJ, 843, 81
Paiano, S., Landoni, M., Falomo, R., Treves, A., & Scarpo, R. 2017, ApJ, 844, 120
Pollack, M., Pauls, D., & Wiita, P. J. 2016, ApJ, 820, 12
Rau, A., Schady, P., Greiner, J., et al. 2012, A&A, 538, 26
Revalski, M., Nowak, D., Wiita, P. J., Wehrle, A. E., & Unwin, S. C. 2014, ApJ, 785, 60
Roberts, D. H., Lehar, J., & Dreher, J. W. 1987, AJ, 93, 968
Romero, G. E., Cellone, S. A., Combi, J. A., & Andruchow, I. 2002, A&A, 390, 431
Ryan, J. L., Siemiginowska, A., Sobolewska, M. A., & Grindlay, J. 2019, ApJ, 885, 12
Sagar, R., Stalin, C. S., Gopal-Krishna, & Wiita, P. J. 2002, MNRAS, 348, 176
Schmidt, G. D., & Smith, P. S. 2000, ApJ, 545, 117
Schonfelder, V., Bennett, K., Blom, J. J., et al. 2000, A&AS, 143, 145
Shakura, N. I., & Sunyaev, R. A. 1973, A&A, 24, 337
Shang, Z., Brotherton, M. S., Green, R. F., et al. 2005, ApJ, 619, 41
Sluse, D., HutsemŽkers, D., Lamy, H., Cabanac, R., & Quintana, H. 2005, A&A, 432, 757
Smith, K. L., Mushotzky, R. F., Boyd, P. T., et al. 2018a, ApJ, 857, 141
Smith, K. L., Mushotzky, R. F., Boyd, P. T., & Wagoner, R. V. 2018b, ApJL, 860, L10
Smith, P. S., Schmidt, G. D., & Allen, R. G. 1993, ApJ, 409, 604
Soldi, S., TŸrler, M., Paltani, S., et al. 2008, A&A, 486, 411
Swanenburg, B. N., Bennett, K., Bignami, G. F., et al. 1978, Natur, 275, 298
Tchekhovskoy, A., Narayan, R., & McKinney, J. C. 2011, MNRAS, 418, L79
Türler, M., Paltani, S., Courvoisier, T. J.-L., et al. 1999, A&AS, 134, 89
Urry, C. M., Scarpa, R., O'Dowd, M., et al. 2000, ApJ, 532, 816
Uttley, P., McHardy, I. M., & Papadakis, I. E. 2002, MNRAS, 332, 231
Van Cleve, J., & Caldwell, D. 2016, Kepler Instrument Handbook KSCI-19033-002 (Moffett Field, CA: NASA Ames Research Center)
Van Cleve, J., Howell, S. B., Smith, J. C., et al. 2016, PASP, 128, 075002
Vanderburg, A., & Johnson, J. A. 2014, PASP, 126, 948
Wehrle, A. E., Carini, M. C., & Wiita, P. J. 2019, ApJ, 877, 151
Wehrle, A. E., Moribito, D. D., & Preston, R. A. 1984, AJ, 89, 336
Wehrle, A. E., Wiita, P. J., Unwin, S. C., et al. 2013, ApJ, 773, 89
Wood, K. S., Meekins, J. F., & Yentis, D. J. 1984, ApJS, 56, 507
Wood, M., Caputo, R., Charles, E., et al. 2017, Proc. ICRC (Busan), 35, 824
Xiong, D., Bai, J., Zhang, H., et al. 2017, ApJ Supp, 229, 21
Xiong, Y., Wiita, P. J., & Bao, G. 2000, PASJ, 52, 1097
Zeng, W., Zhao, Q.-J., Dai, B.-Z., et al. 2018, PASP, 130, 024102
Zhang, X.-H., & Bao, G. 1991, A&A, 246, 21
Zhang, Z.-X., Du, P., Smith, P. S., et al. 2019, ApJ, 876, 49